Synthetic Tunability of Colloidal Covalent Organic Framework/Nanocrystal Hybrids

Yannick T. Guntern[†], Jan Vávra[†], Vikram V. Karve[§], Seyedeh Behnaz Varandili[†], Ona Segura Lecina[†], Chethana Gadiyar[†], and Raffaella Buonsanti[*†]

[†] Laboratory of Nanochemistry for Energy (LNCE), Institute of Chemical Sciences and Engineering (ISIC), École Polytechnique Fédérale de Lausanne, CH-1950 Sion, Switzerland.

[§] Laboratory for Functional Inorganic Materials (LFIM), Institute of Chemical Sciences and Engineering (ISIC), École Polytechnique Fédérale de Lausanne, CH-1950 Sion, Switzerland.

*Correspondence to: raffaella.buonsanti@epfl.ch

ABSTRACT

The combination of porous reticular frameworks and nanocrystals (NCs) offers a rich playground to design materials with functionalities, which are beneficial for a large variety of applications. Achieving compositional and structural tunability of these hybrid platforms is not trivial and new approaches driven by the understanding of their formation mechanism are needed. Here, we present a synthetic route to encapsulate NCs of various sizes, shapes and compositions in the microporous imine-linked covalent organic framework (COF) LZU1. The tunable NC@LZU1 core-shell hybrids are synthesized by combining colloidal chemistry and homogenous microwave-assisted syntheses, an approach which allows the tailoring of the shell thickness while ensuring COF crystallinity in the presence of the NCs. The uniform morphologies of these new composite materials along with their colloidal nature enable insights into their formation mechanism. Having learned that the COFs heterogeneously nucleate on the NC seeds, we further expand the synthetic approach by developing a step-by-

step encapsulation strategy. Here, we gain control over the spatial distribution of various NCs within multi-layered NC@LZU1@NC@LZU1 core-shell-core-shell hybrids and we also form yolk-shell nanostructures. The synthetic route is general and applicable to a broad variety of NCs (with catalytic, magnetic or optical properties), thus revealing a new way to impart functionalities to COFs.

INTRODUCTION

Covalent organic frameworks (COFs) are porous, crystalline, extended structures which are solely composed of light elements and held together by strong covalent bonds.[1,2] The reticulation of two distinct molecular building blocks into such 2D or 3D frameworks has become a very active research area in chemical science due to the enormous possibilities offered by these new materials. To realize their full potential towards applications, COFs have to be synthesized as processable materials, which is a major challenge considering that the most common synthesis procedures form insoluble and difficult to process microcrystalline powders.[3] Recent studies have shown that controlling the size of COFs in the tens of nanometer length scale is key to obtain colloidal solutions; the latter are both easy to process and also facilitate mechanistic studies of reaction pathways.[4–8] As an additional advantage, the controlled growth of COF nanoparticles makes them compatible to form composites with other nanomaterials. Among the different classes of materials, colloidal inorganic nanocrystals (NCs) are ideal candidates to further expand the functionalities and potential applications of COFs as they possess a superior tunability of the physical and chemical properties thanks to the precise control of their size, shape and composition which is achievable to date.[9–11] Indeed, the encapsulation of colloidal NCs within porous reticular frameworks, including metal-organic frameworks (MOFs) and COFs, has been demonstrated to generate synergistic interactions and to infer new functionalities which are beneficial for various applications, including catalysis, sensing or separations.[12–20]

In previous studies, NC/COF hybrids have been synthesized by solution impregnation or chemical vapour infiltration of metal precursors into the pores of pre-synthesized COFs and subsequent reduction to form NCs.[21–30] However, in this template-directed approach, the COF pores limit the freedom in the NC size and shape tunability. Such drawback can be overcome by using pre-synthesized NCs as nucleation seeds for the COF growth; yet, this approach is challenged by the harsh conditions required to crystallize COFs.[31] Few studies have demonstrated the formation of NC@COF (where "@" indicates NCs embedded in the COF to form core-shell structures) hybrids via a two steps approach wherein an amorphous shell is formed first and it is converted into a crystalline framework by subsequent treatments.[32–34] While the direct encapsulation of NCs into crystalline COFs has been more recently proved to be a valid alternative, the compositional diversity and the control over the spatial distribution of one or multiple types of NCs within a crystalline COF matrix is still limited.[35–37] Moreover,

while essential to expand the accessible library of these new composite materials, a detailed understanding of the formation process of these hybrids is missing.

Herein, we describe the synthesis of colloidal NC/COF hybrids including NCs of various sizes, shapes and compositions embedded in the microporous imine-linked COF LZU1 with control over the spatial distribution of the two components.[38] LZU1 was chosen for two reasons. First of all, this 2D layered framework possesses well-defined pore channels and exhibits an outstanding water stability,[39] which makes it an ideal candidate to host metallic NCs for e.g. catalytic applications including waste water treatments.[40,41] Furthermore, LZU1 can be nanosized through a homogenous microwave-assisted synthesis;[5] such approach increases the compatibility of the colloidal NC and COF chemistry. Our synthesis method allows to obtain a crystalline porous COF shell around NC cores (NC@LZU1 hybrids) and to precisely tune its thickness in just one single step. We then combine this seeded-growth with a subsequent functionalization of the COF shell with NCs to synthesize NC@LZU1@NC@LZU1 core-shell-core-shell structures in the form of colloidal solutions. We also demonstrate that NC@LZU1 yolk-shell hybrids can be produced with an additional treatment. The as-prepared hybrids exhibit all the functionalities deriving from the embedded NCs, including optical, magnetic and catalytic activity.

RESULTS AND DISCUSSION

Colloidal NCs of different size, shape and composition were synthesized by previously reported methods (**Figure S1**). The original ligands were substituted with polyvinylpyrrolidone (PVP) for all the as-synthesized NCs in order to assure the same surface chemistry while dispersing them in ethanol for the subsequent encapsulation process. Fourier transform infra-red (FTIR) spectroscopy confirmed the presence of PVP on the NC surface (**Figure S2**). This specific amphiphilic surfactant polymer was chosen because it is also employed as a capping agent for the formation of nanosized LZU1. The synthesis of the COF shell was initially demonstrated and optimized on spherical Au NCs (11.7 ± 1.2 nm, **Figure S1a**) by adapting a previously reported procedure for the synthesis of nanosized LZU1.[5] Here, to slow down the imine condensation reaction and facilitate the COF crystallization, the amine precursor 4-(*tert*-butoxycarbonylamino)-aniline (NBPDA) is gradually deprotected with trifluoroacetic acid (TFA) and reacted with triformylbenzene (TFB). Typically, TFB (10 mg, 0.06 mmol), NBPDA (20 mg, 0.1 mmol) and PVP (MW = 360,000, 20 mg) were dissolved in ethanol (2 mL) and

mixed with TFA (0.24 mL) and Au NCs (0.5 mL of 0.3 mg/mL Au in ethanol). The homogenous mixture was then reacted under microwave irradiation at 120 °C for 30 min. **Figure 1** illustrates the overall synthetic procedure.

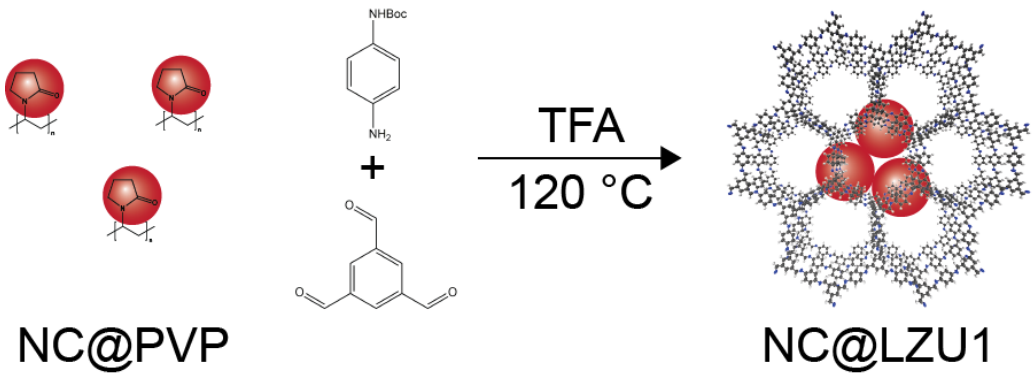

Figure 1. Scheme illustrating the synthesis of NC@LZU1 hybrids. PVP-modified NCs of various sizes, shapes and compositions are encapsulated in the COF LZU1 by a microwave-assisted solvothermal synthesis. TFA gradually deprotects the COF linker (NBPDA) and serves as catalyst for the imine condensation with the second linker (TFB).

Scanning electron microscopy (SEM, **Figure 2A** and **B**) and transmission electron microscopy (TEM, **Figure 2D** and **S3**) images reveal the formation of Au@LZU1 hybrids, in which multiple Au NCs are embedded in a uniform COF shell with an average diameter of 373 ± 41 nm. The yield of the hybrids (i.e. the fraction of COF particles containing Au NC cores) is greater than 90%. The average size of the Au NCs (11.0 ± 1.9 nm) was retained during the encapsulation. The crystallinity and phase purity of the COF shell was confirmed by low-angle selected area electron diffraction (SAED) (**Figure 2D**, inset) and powder X-ray diffraction (PXRD) (**Figure 2C**). Compared to the intense diffraction peaks originating from LZU1, the Au NCs showed only very weak and broad diffraction peaks due to their small size and low concentration in the hybrids (**Figure 2C**, inset). Furthermore, the presence of the Au NC cores was confirmed by high-angle annular dark-field scanning TEM (HAADF-STEM) (**Figure 2E**) and the corresponding energy dispersive X-ray spectroscopy (EDX) elemental map (**Figure 2F**).

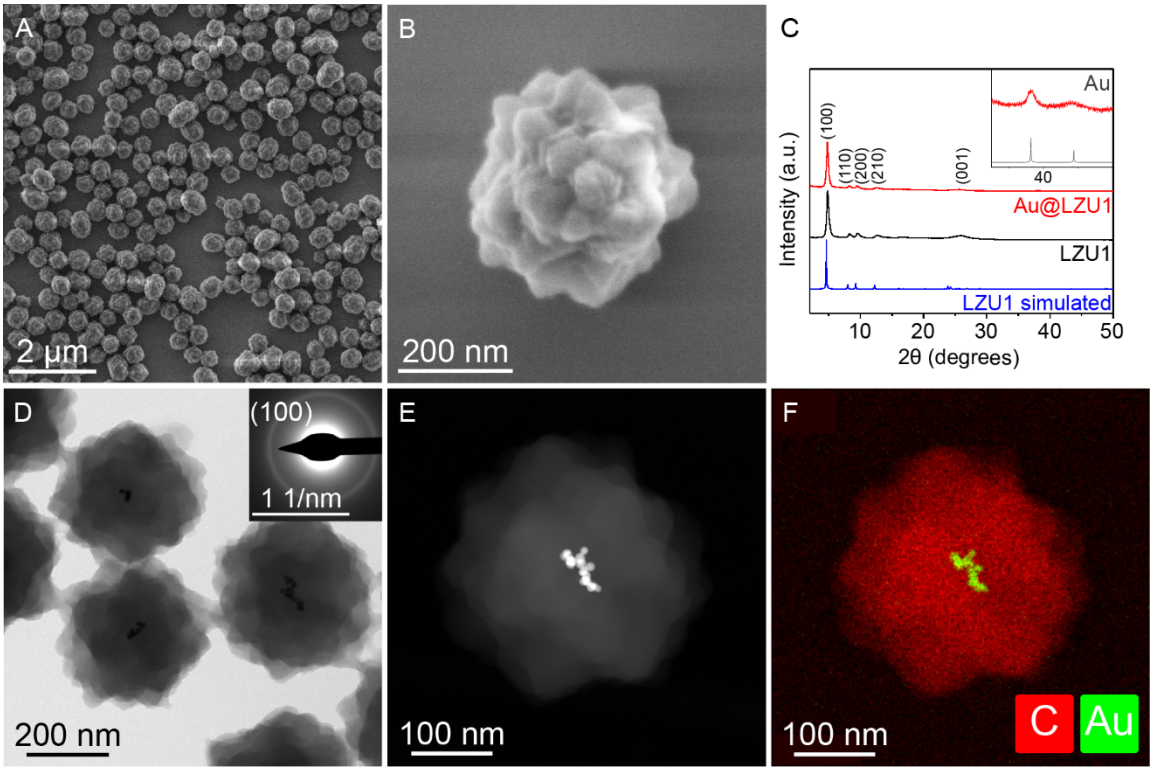

Figure 2. Electron microscopy and PXRD characterization of the Au@LZU1 hybrids. (A) Low- and (B) high-magnification SEM images of Au@LZU1 hybrids containing Au nanospheres. (C) PXRD patterns (λ=1.5406 Å) of LZU1 (black) and Au@LZU1 (red) together with the simulated pattern for LZU1 (blue, simulated from crystallographic data in ref 38) and Au (grey inset, ICSD-52700). (D) TEM image with corresponding SAED pattern (inset) of Au@LZU1 hybrids. (E) HAADF-STEM image and (F) corresponding EDX elemental map of Au@LZU1.

To gain insights into the 3D structure and morphology of the NC@LZU1 hybrids, we performed high-resolution TEM (HRTEM) tilt series experiments. The images were acquired with a low electron dose (150 e^{-} nm^{-2} per image) to minimize electron beam damage of the COF.[42,43] **Figure 3 A–C** shows three selected segments of a tilt series which was performed on the Au@LZU1 hybrids. The images evidence a uniform 3D morphology with the Au NCs centered in the core of the COF (**Figure S4, Supplementary Movie 1**). Moreover, this analysis confirms the high crystallinity of the hybrids, which are constructed by multiple crystalline domains showing phase contrast (d-spacing of ~1.8 nm) which matches well the 1D channels of LZU1.[35] The high-magnification images in **Figure 3D–F** reveal that the pore channels are arranged along the radial direction of the COF shell and pointing towards the Au NC cores.

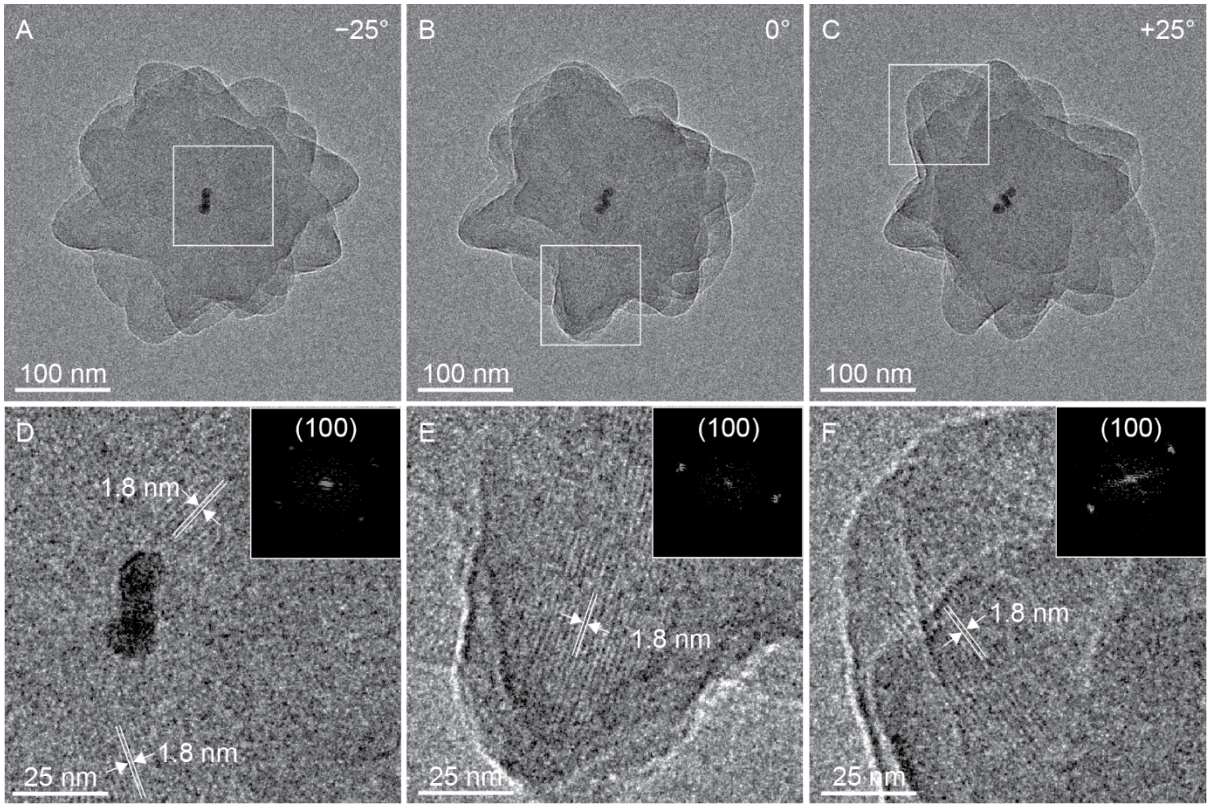

Figure 3. Low dose HRTEM characterization of Au@LZU1. TEM tilt series of Au@LZU1 hybrid acquired with a low electron dose (150 e^{-} nm^{-2} per image) and 5° increment steps from –50° to 50° with selected images at (A) –25°, (B) 0° and (C) +25°. The Au@LZU1 hybrids used here (329 ± 40 nm) were synthesized with a shorter reaction time (15 min) to decrease the shell thickness and thus obtain a better insight into the core area due to lower thickness contrast. (D) High-magnification image corresponding to the white square in (A) showing the phase contrast from two different crystalline domains close to the Au NC core. (E) High-magnification image corresponding to the white square in (B) showing the phase contrast of a crystalline domain at the periphery of the COF shell. (F) High-magnification image corresponding to the white square in (C). The inset in (D), (E) and (F) shows the fast Fourier transform (FFT) of the respective image with a d-spacing of ~1.8 nm corresponding to the (100) planes of LZU1.

Having assessed the successful formation of the Au@LZU1 hybrids, we investigated the role of different reaction parameters on the final morphology. Increasing the concentration of the COF precursors (TFB and NBPDA), while keeping all the other reaction parameters constant, resulted into progressively thicker COF shells, from an average size of 105 ± 18 nm to 617 ± 78 nm (**Figures 4B–F**). When the amounts of TFB and NBPDA are decreased down to 2.5 and 5 mg, respectively, a qualitative assessment of TEM images evidences that the

majority of the NCs is not encapsulated and only a few Au@LZU1 hybrids are found. This observation indicates that these amounts are the lower limits for the specific NC concentration used in this synthesis (**Figure 4A**). The absence and very weak intensity of the (100) diffraction signal in the SAED patterns in **Figure 4B** and **C**, respectively, indicates that thinner shells are less crystalline.

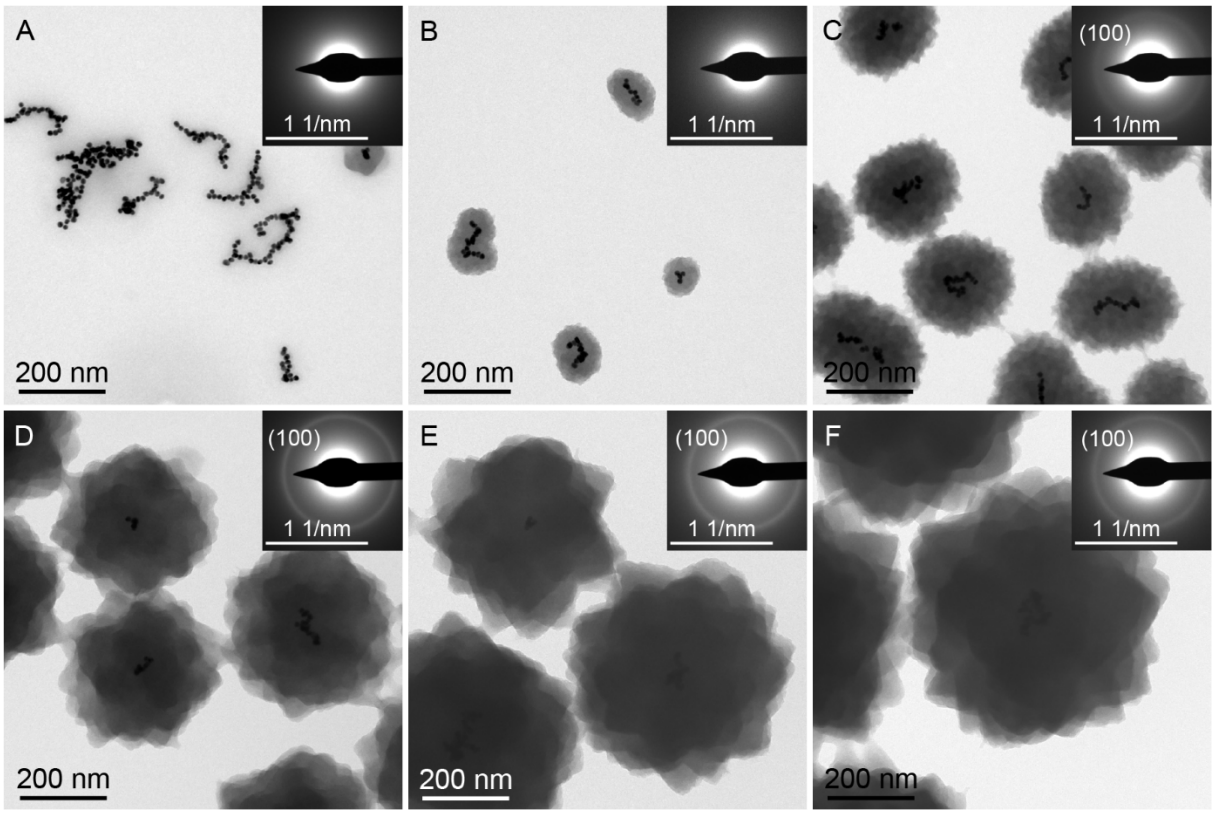

Figure 4. Size tunability of Au@LZU1 hybrids by COF precursor concentrations. TEM images with corresponding SAED patterns (insets) of Au@LZU1 samples containing Au nanospheres and an average COF shell diameter of (A) 0 nm, (B) 105 ± 18 nm, (C) 226 ± 23 nm, (D) 373 ± 41 nm, (E) 539 ± 52 nm and (F) 617 ± 78 nm, synthesized by varying the TFB/NBPDA amounts in the COF precursor solution: (A) 2.5/5 mg, (B) 5/10 mg, (C) 7.5/15 mg, (D) 10/20 mg, (E) 15/30 mg and (F) 20/40 mg.

Longer reaction times or lower NC concentrations, while keeping all the other reaction parameters constant, result in a similar increase of the shell thickness and crystallinity (**Figures 5** and **S5**). Additionally, as previously reported for pure LZU1, a decrease in the concentration of the surface passivating PVP can further regulate the COF growth and thus yield larger hybrids (**Figure S6**).[5]

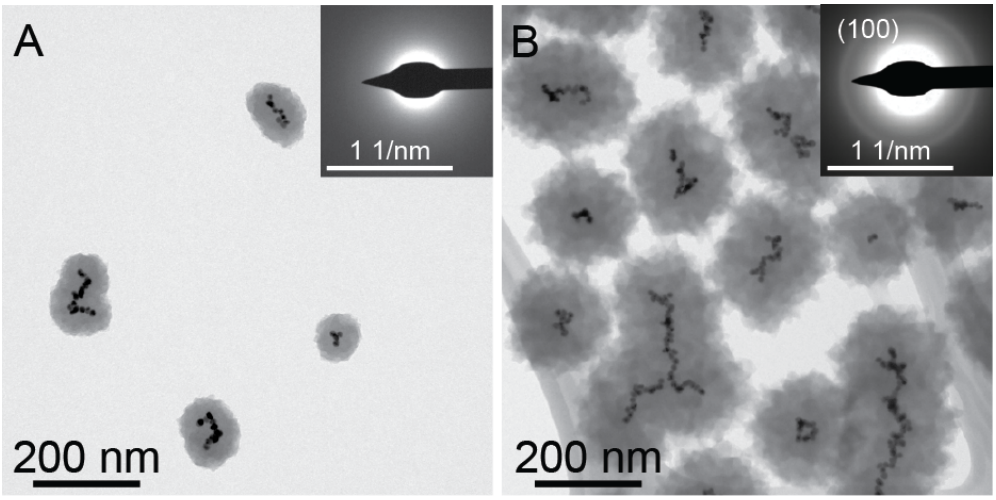

Figure 5. Size tunability of Au@LZU1 hybrids by reaction time. TEM images with corresponding SAED patterns (insets) of Au@LZU1 hybrids containing Au nanospheres and synthesized with decreased TFB/NBPDA amounts (2.5 mg/ 5 mg) and reaction times of (A) 30 min (105 ± 18 nm) and (B) 60 min (201 ± 27 nm).

Based on all the above results, a mechanistic picture for the formation of the NC@LZU1 hybrids starts to emerge (**Figure 6**). The finding that the final size of the COF shell is affected by the NC concentration (**Figure S5**) and the high yield of hybrids (>90%) is consistent with the role of the NCs as nucleation seeds for LZU1. Indeed, the lower the number of seeds is, the thicker the final COF shell is expected as less precursors are consumed during the nucleation phase. Moreover, Au@LZU1 hybrids are smaller and have a narrower size distribution (373 ± 41 nm) compared to blank LZU1 (1354 ± 320 nm, **Figure S7**) synthesized under the same conditions in the absence of NCs, which further indicates that the NCs act as seeds for the COF growth.[20]

As a reminder, the NCs are functionalized with PVP. This amphiphilic surfactant polymer serves a double role: it stabilizes the NCs in the ethanolic growth solution and it also acts as a capping agent for the controlled COF growth. While it was not possible to get any insight by FTIR spectroscopy or HRTEM into the interface between the PVP molecules adsorbed on the NC surface and the COF shell, previous studies on NC/MOF hybrids based on a similar encapsulation strategy have suggested that it may act as a binder between the NCs and the reticular framework.[12,36] Based on those and on our findings, we propose that the shell nucleates on the PVP-coated NCs, initially as an amorphous phase or as 2D disordered sheets, which then transform into a crystalline porous framework while the growth proceeds, which is confirmed by the SAED patterns in **Figures 4** and **5**. FTIR measurements are consistent with

such hypothesis (**Figure S8**). The existence of the polymerization and crystallization as two separate processes agrees also with previous literature on imine-linked 2D COFs.[7,44–47] Furthermore, one study on heterogeneous growth of LZU1 on silica spheres reports a similar finding, although their approach is a two-step rather than a one-step encapsulation.[48]

Interestingly, the HRTEM tilt series (**Figure 3**) evidences that the COF pores are aligned in the direction of the NCs. This finding suggests that during the crystallization stage the COF crystallites undergo a radial growth via π-π stacking of individual LZU1 layers. Similar preferred growth in the π-π stacking direction was previously observed in other studies on 2D imine-linked COFs.[44,49] Specifically, a substrate-supported growth has been shown to reinforce the stacking of LZU1 layers parallel to the surface plane, independently from the existence of a particular crystallographic relationship with the substrate.[44] The NCs might have a similar impact on the COF growth in the NC@COF hybrids.

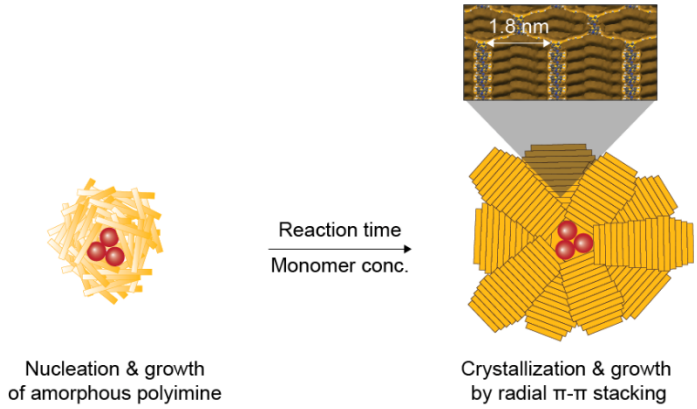

Figure 6. Schematics of the COF formation mechanism in the NC@COF hybrids.

Having learned about the formation mechanism of the Au@LZU1 hybrids, we explored the generality of the synthesis approach and expanded it further. To increase the complexity and to control the spatial distribution of various NCs within the COF matrix, which can be beneficial for size-selective catalysis[14] or for engineering charge transfer schemes within the composites, we developed a step-by-step encapsulation strategy. Au nanospheres were immobilized on pre-synthesized Au@LZU1 hybrids containing Au nanorod cores (length: 141.5 ± 6.1 nm, diameter: 60.5 ± 3.7 nm) (**Figure 7A**) by mixing them under sonication. The TEM image of the resulting Au@LZU1@Au composite in **Figure 7B** confirms the deposition of Au nanospheres on the surface of the COF shell. To form a second COF shell, the as-synthesized Au@LZU1@Au hybrids were then simply mixed with the LZU1 precursors and reacted for 5 minutes. The TEM image (**Figure 7C**) and the HAADF-STEM image with

corresponding EDX elemental maps (**Figure 7D**) confirm the formation of the Au@LZU1@Au@LZU1 core-shell-core-shell structure. The COF crystallinity and phase purity of the multi-layered composite was confirmed by SAED (**Figure 7C**, inset); the weaker diffraction intensity compared to the initial Au@LZU1 hybrids (**Figure 7A**, inset) reveals a lower crystallinity in the outer shell due to the shorter reaction time used here.

We also used colloidal NCs of various sizes, shapes and compositions for the formation of NC@LZU1 hybrids to demonstrate the generality of the developed synthetic approach. To this end, triangular Au nanoplates (edge length: 174.1 ± 20.0 nm), WO_3 nanowires (length: 53.3 ± 14.5 nm, diameter: 4.1 ± 1.2 nm) and Fe_3O_4 nanospheres (15.0 ± 0.9 nm) were synthesized (**Figure S1**). To encapsulate the different NCs in the COF shell, the same approach previously discussed was applied. The TEM images of the resulting hybrid structures (**Figures 7E–G**) confirm the growth of the COF shell around the various NCs and reveal that their size and shape were mostly retained. It has to be mentioned here that the initial concentrations of the NCs in the reaction solution were not optimized for these experiments, which explains the varying thickness of the COF shell and differing number of encapsulated NCs between the samples. The prepared hybrids are highly dispersible in ethanol and remain stable for more than six months by storing at room temperature with no evidence of aggregation, meaning that they sediment over time but can be redispersed simply by shaking.

Furthermore, CdSe QDs (2.5 nm, **Figure S1f**) were deposited on Au@LZU1 hybrids (with Au nanosphere cores), with the only difference that the immobilization was performed by stirring in a N_2 glove box to avoid air-exposure of the QDs. **Figure 7H** shows the obtained Au@LZU1@CdSe hybrid with a uniform outer layer of CdSe QDs and demonstrates that our step-by-step encapsulation strategy can be applied to multiple types of colloidal NCs.

Moreover, the good dispersibility of our hybrids allowed us to prepare yolk-shell nanostructures, which are very attractive for catalysis.[34] By simply adding TFA to an ethanolic solution of Au@LZU1 hybrids (containing Au nanospheres) and reacting at 120 °C for 20 min, we obtained yolk-shell Au@LZU1 hybrids with retained COF crystallinity shown in **Figure 7I**. The formation of the hollow cavity around the Au nanospheres can be ascribed to an inside-out Ostwald ripening, which was previously reported for the formation of hollow 2D imine COFs.[49,50] It should be noted that, while our synthetic approach allows precise tuning of the shell thickness while ensuring COF crystallinity in the presence of NCs, the experimental setup limits us to control the COF nucleation on one single NC, which might be possible to achieve in the future by controlled precursor addition e.g. with a syringe pump.[20]

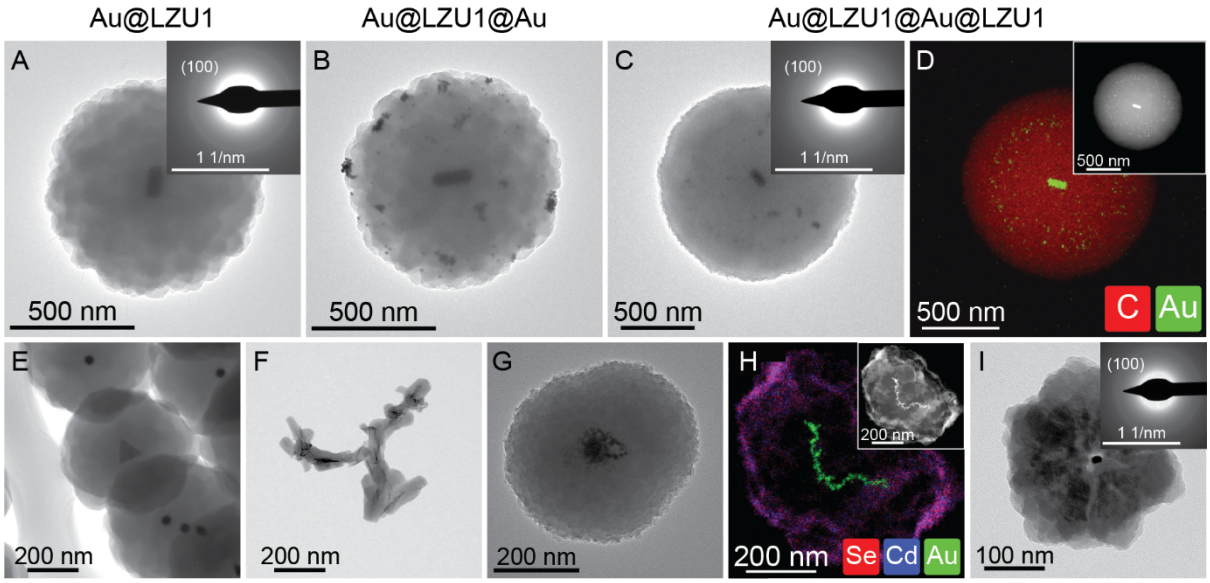

Figure 7. Control over the spatial distribution of NCs in the COF matrix and general applicability of the synthetic approach. (A–D) Step-by step encapsulation strategy to form core-shell-core-shell hybrids. TEM images with corresponding SAED patterns (insets) of (A) Au@LZU1 hybrids containing Au nanorods, (B) Au@LZU1@Au and (C) Au@LZU1@Au@LZU1 hybrids containing Au nanorods and Au nanospheres in the inner and outer core, respectively. (D) EDX elemental map and corresponding HAADF-STEM image (inset) for Au@LZU1@Au@LZU1. (E–G) TEM images of NC@LZU1 samples containing (E) Au triangular nanoplates, (F) WO_3 nanowires and (G) Fe_3O_4 nanospheres. (H) EDX elemental map and corresponding HAADF-STEM image (inset) for Au@LZU1@CdSe hybrid containing Au nanospheres in the inner core and CdSe QDs immobilized on the LZU1 shell. (I) TEM image of yolk-shell Au@LZU1 hybrid containing Au nanospheres with corresponding SAED pattern (inset).

Finally, we assessed the functional properties of the NC@LZU1 hybrids (**Figure 8**). The porosity and surface area of Au@LZU1 hybrids were measured by N_2 sorption analysis at 77 K and compared to a blank LZU1 sample synthesized under the same conditions in the absence of NCs (**Figures 8A, S9**). High surface areas of 1388 m^2/g and 1066 m^2/g were obtained for LZU1 and Au@LZU1, respectively, by applying the Brunauer-Emmett-Teller (BET) model. Both, the hybrids and blank LZU1 display type I isotherms with a steep increase in N_2 uptake at low relative pressure (<0.01) indicating microporosity. The steeper tail end of the uptake curve for Au@LZU1 compared to LZU1, indicates the presence of larger macropores/intercrystalline pores in the hybrids.[51] However, the encapsulation of the NCs in the COF does not impact the pore-size distribution (**Figure S9b**). Indeed, both samples reveal

a pore width of ~1.3 nm indicating that the incorporated NCs do not occupy the pores of the LZU1 matrix due to their larger size. Considering that the wt% of Au in the Au@LZU1 hybrids is only around 1%, this finding suggests that most of the decreased gravimetric BET surface area in the Au@LZU1 hybrids (~ 23%) must be related to larger macropores in between the grains.[51]

To study the accessibility of the encapsulated NCs in the COF matrix for eventual catalytic reactions, we used the reduction of methylene blue (MB) dye with $NaBH_4$ in aqueous solution as a model reaction.[40,41,52–54] The reaction progress was monitored via UV-Vis absorption spectroscopy by following the decrease in the characteristic absorption peak of MB (λ_{max} = 664 nm). **Figure 8B** reports the results after 5 minutes for Au NCs, LZU1 and the Au@LZU1 hybrids compared to the MB blank. The monitoring over longer times is shown in **Figure S10**. The observation that the hybrids do catalyze the reduction of the dye indicate that the MB molecule can diffuse through the pores of LZU1 (as it was previously demonstrated for LZU1 membranes)[39] and react on the surface of the Au NCs. It should be noted that some of the pores are likely blocked by the interfacial PVP and the intergrowth of COF crystallites on the NC seeds, which are not all aligned perpendicular to the NC surface. This can explain the lower catalytic activity of the hybrids compared to blank Au NCs in addition to mass-transfer effects imposed by the porous shell. **Figure S11** shows that the conversion efficiency is mostly retained during five cycles.

In addition to catalytic activity, the integration of QDs provides an opportunity to impart optical properties to COFs or to extend their existing absorption range. Thus, we immobilized CdSe QDs on pre-synthesized blank LZU1 (**Figure S13**) and measured the UV-Vis absorption spectrum of the resulting LZU1@CdSe hybrid, which is shown in **Figure 8C**. In future experiments, the spatial control of different NCs within the COF matrix, could open up a new avenue to study distance dependent excitation energy-transfer between light-harvesting QDs and plasmonic metal NCs.[55] However, the intrinsic broad UV-Vis absorption of LZU1 is not ideal here, so a different COF should be used for this purpose.

Finally, **Figure 8D** shows that the Fe_3O_4@LZU1 composites (**Figure 7G**) can be collected from a colloidal suspension by applying a magnetic field. The residual slightly yellow colour in the supernatant can be attributed to a small amount of LZU1 crystallites without incorporated Fe_3O_4 NCs. Nevertheless, this experiment proves that magnetic properties can be conferred to the COF via incorporation of magnetic NCs

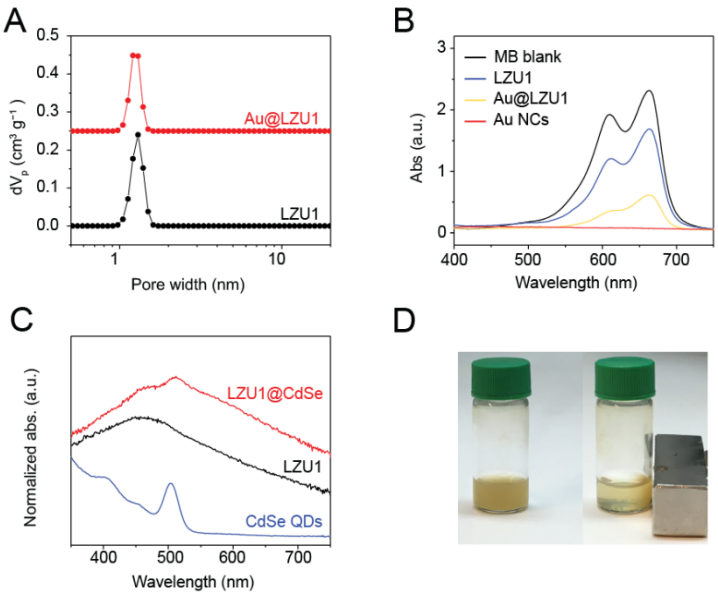

Figure 8. Porosity, catalytic, optical and magnetic properties of NC/COF hybrids. (A) N_2 sorption isotherms for blank LZU1 (black) and Au@LZU1 hybrids (red), containing 1.03 wt% Au nanospheres, at 77 K up to 1 bar. (B) UV-Vis spectra of methylene blue (MB) after reduction with $NaBH_4$ for 5 min without catalysts (black), in the presence of blank LZU1 (blue), Au@LZU1 (yellow) and Au NCs (red). (C) UV-Vis spectra of LZU1@CdSe (red), LZU1 (black) and CdSe QDs (blue). (D) Photo of Fe_3O_4@LZU1 hybrids collected by applying a magnetic field (right) to the colloidal suspension (left).

CONCLUSIONS

In summary, we have developed a new synthetic route to synthesize NC/COF hybrids with various types of colloidal NCs and controllable thickness of the LZU1 shell. A HRTEM tilt series allowed us to get a better insight into the 3D structural morphology of the hybrids. Together with the observed reaction parameter dependent trends, we were able to deepen our understanding of the hybrid formation mechanism. The initial heterogeneous nucleation of an amorphous polyimine is followed by the crystallization of the COF, which then preferentially grows in the radial direction from the NC cores via π-π stacking of the 2D layers.

The colloidal nature of the hybrids allowed us to go a step further and design a sequential encapsulation of NCs with multiple size, shape, composition and controlled spatial distribution within the same COF matrix and also to prepare yolk-shell nanostructures. The catalytic activity of the Au@LZU1 hybrids towards the MB dye reduction serves as a proof of the molecular accessibility to the NC cores, which are embedded in the highly crystalline and

porous COF shell. In the future, new strategies are foreseen to create a clean interface between the NC core and the COF shell, for example by substituting the PVP with one of the COF linkers as the stabilizer. Moreover, we show that our method is general and applicable to prepare hybrids with other functionalities that derive from the incorporated NCs as e.g. optical and magnetic properties. Going a step further, our approach could potentially be expanded to the formation of composites with other COFs which are constructed by Schiff-base reactions as e.g. highly stable *β*-ketoenamine-linked COFs.[3,6,55] Overall, our synthetic route contributes to a better understanding of the formation processes of NC/COF hybrids and might open up a new avenue for the design of new composite materials with beneficial synergistic interactions, as for example exciton-plasmon coupling or tandem catalysis.[56–58]

EXPERIMENTAL SECTION

Chemicals. Polyvinylpyrrolidone (PVP, MW = 360,000), triethylamine (TEA, ≥ 99.5%), ethanol (EtOH, anhydrous, 95%), nitric acid (HNO_3, 70%, 99.999% trace metals basis) and hydrochloric acid (HCl, 37%, 99.999% trace metals basis) were purchased from Sigma-Aldrich. 1,3,5-Triformylbenzene (TFB, 98%), 4-(*tert*-butoxycarbonylamino)-aniline (NBPDA, ≥ 97%) and trifluoroacetic acid (TFA, 99.5%) were purchased from Acros Organics. All chemicals were used as received without further purification.

Synthesis of COF/NC hybrids. *NC@LZU1.* The synthesis of the COF shell in the presence of NCs (see SI for NC synthesis) was performed by adapting a previously reported procedure for the preparation of LZU1 in a synthWave 1500 microwave high pressure reactor.[5] In a typical synthesis (for crystalline hybrids with a size of 373 ± 41 nm), TFB (10 mg, 0.06 mmol), NBPDA (10 mg, 0.1 mmol) and PVP (MW = 360,000, 20 mg) were dissolved in 2 mL of EtOH by sonication and mixed with 0.24 mL of TFA and 0.5 mL of NC solution in EtOH (0.3 mg/mL). The mixture was transferred to a microwave glass vial (10 mL), quickly heated to 120 °C (within 5 min), kept at 120 °C for 30 min and slowly cooled down to room temperature (over 60 min). After the reaction, the red colloid was diluted with EtOH to 10 mL and centrifuged at 11,500 rpm for 10 min. The precipitated hybrids were dispersed in 8 mL of EtOH and 0.5 mL of TEA was added to deprotonate the imine in LZU1, which is indicated by a color change from red to yellow.[5] The hybrids were precipitated by centrifugation at 11,500 rpm for 10 min and re-dispersed into EtOH. The COF shell thickness was tuned by individually changing the TFB/NBPDA concentrations (**Figure 4**), the reaction time (**Figure 5**), the NC concentration

(**Figure S5**) or the PVP concentration (**Figure S6**), while keeping all the other reaction parameters constant (if not specifically mentioned). Blank LZU1 particles were synthesized without the addition of NCs to the reaction mixture (**Figure S7**).

NC@LZU1@NC@LZU1. PVP-capped NCs in EtOH (0.5 mL) were mixed with as-synthesized blank LZU1 or NC@LZU1 hybrids in EtOH (0.5 mL) and sonicated for 60 min, as previously demonstrated for the immobilization of NCs on MOFs.[13] The resulting LZU1@NC or NC@LZU@NC hybrids were washed with EtOH (1 mL) three times by centrifugation for 5 min at 13,300 rpm and recovered in EtOH (0.5 mL). To grow an additional COF shell around the immobilized NCs, the same procedure described above was applied by simply adding the LZU1@NC or NC@LZU@NC hybrids in EtOH (0.5 mL) to the COF precursor solution.

Yolk-shell NC@LZU1. Yolk-shell Au@LZU1 nanostructures were prepared by adding TFA (0.24 mL) to an ethanolic solution of Au@LZU1 hybrids (2 mL) and reacting the mixture for 20 min in a synthWave 1500 microwave high pressure reactor. After the reaction, the red colloid was diluted with EtOH to 10 mL and centrifuged at 11,500 rpm for 10 min. The precipitated yolk-shell hybrids were dispersed in 8 mL of EtOH and 0.5 mL of TEA was added to deprotonate the imine in LZU1, which is indicated by a color change from red to yellow.[5] The hybrids were precipitated by centrifugation at 11,500 rpm for 10 min and re-dispersed into EtOH.

Characterization. *Electron Microscopy.* Transmission electron microscopy (TEM) images and selected area electron diffraction (SAED) patterns were acquired on a FEI Tecnai-Spirit at 120 kV. The SAED patterns were obtained from 415 μm^2 areas. The high-resolution TEM (HRTEM) tilt series was acquired on a FEI Tecnai F20 Cryo at 200 kV. High-angle annular dark-field scanning TEM (HAADF-STEM) images and energy dispersive X-ray spectroscopy (EDX) elemental maps were acquired on a FEI Talos at 200 kV. Samples were prepared by drop-casting colloidal solutions of the NCs/hybrids on the surface of carbon-coated Cu or Au grids (Ted Pella, Inc.). Scanning electron microscopy (SEM) images were acquired on a FEI Teneo, using an in-lens (Trinity) detector at a beam energy of 2 keV and a beam current of 13 pA. Samples were prepared on conductive p-doped silicon substrates. Size statistics were performed using ImageJ software and counting at least 50 NCs/hybrids per sample.

UV-Vis Absorption Spectroscopy. UV-Vis absorption spectroscopy was performed in transmission mode using a Perkin Elmer Lambda 950 Spectrophotometer equipped with a deuterium lamp as a light source for the ultraviolet range and a tungsten halide lamp as a light source for the visible and infrared ranges, as well as a photomultiplier tube (PMT) with a

Peltier-cooled PbS detector. The samples were prepared in a quartz cuvette and the background signal of the used solvent was subtracted.

Powder X-ray Diffraction (PXRD). The PXRD patterns were acquired on a Bruker D8 Advance diffractometer with a Cu Kα source (λ = 1.5406 Å) and a Lynxeye one-dimensional detector, which was operated at 40 kV and 40 mA. The powder samples were obtained by drying the COF or hybrid colloidal solutions under N_2 flow and prepared on Si low background sample holders. Simulated XRD patterns were generated by using Mercury software (CSD, version 2020.1).). It should be mentioned that the amount of sample obtained from one single synthesis is too low to obtain good quality PXRD data. The products of multiple syntheses must be collected for this measurement. For this reason, we rely on SAED patterns for most of the samples discussed in the manuscript.

Gas sorption measurements. Nitrogen adsorption measurements were done on a Belsorp Max device. Samples (50–100 mg) were activated at 120 °C under dynamic vacuum for 12 h. N_2 isotherms were obtained using incremental exposure of ultra-high purity N_2 in a liquid N_2 dewar at 77 K. The specific surface area was calculated by the BET method between a P/P_0 range of 0.008–0.2. As for PXRD, the products of multiple syntheses must be collected to obtain enough sample for good quality gas sorption data.

Attenuated Total Reflectance Fourier-Transform Infrared Spectroscopy (ATR-FTIR). ATR-FTIR was performed using a Perkin Elmer Spectrum Two FTIR Spectrometer. Samples were prepared by drop-casting colloidal solutions of the NCs/hybrids and evaporating the solvent on the sample holder and measured with a resolution of 4 cm^{-1}. Air background measurements were subtracted from the spectra.

Inductively Coupled Plasma Optical Emission Spectrometry (ICP-OES). ICP-OES was performed on an Agilent 5100 model to determine the NC concentrations. Five standard solutions of the respective element were prepared to obtain the calibration curve used to determine the concentrations of the digested NC solution. The sample solution was prepared by dissolving the NCs in 70% HNO_3 followed by the addition of a specific volume of DI H_2O until the solution reached the 2% HNO_3 concentration needed for the analysis. Au NCs were dissolved in aqua regia (1:1 mixture of 70% HNO_3 and 37% HCl) followed by the addition of a specific volume of DI H_2O until the solution reached the 2% HNO_3, 1% HCl concentration needed for the analysis.

ASSOCIATED CONTENT

Supporting Information

The Supporting Information is available free of charge on the ACS Publications website (link): Experimental details, additional TEM images, FTIR and UV-Vis spectra and gas sorption isotherms (PDF)

ACKNOWLEDGEMENTS

This work was mostly supported by the ERC Starting Grant HYCAT with agreement number 715634. The authors thank Robin Girod for technical assistance with the acquisition of the HRTEM tilt series.

REFERENCES

(1) Diercks, C. S.; Yaghi, O. M. The Atom, the Molecule, and the Covalent Organic Framework. *Science* **2017**, *355*, eaal1585.

(2) Lyle, S. J.; Waller, P. J.; Yaghi, O. M. Covalent Organic Frameworks: Organic Chemistry Extended into Two and Three Dimensions. *Trends Chem.* **2019**, *1*, 172–184.

(3) Kandambeth, S.; Dey, K.; Banerjee, R. Covalent Organic Frameworks: Chemistry beyond the Structure. *J. Am. Chem. Soc.* **2019**, *141*, 1807–1822.

(4) Smith, B. J.; Parent, L. R.; Overholts, A. C.; Beaucage, P. A.; Bisbey, R. P.; Chavez, A. D.; Hwang, N.; Park, C.; Evans, A. M.; Gianneschi, N. C.; Dichtel, W. R. Colloidal Covalent Organic Frameworks. *ACS Cent. Sci.* **2017**, *3*, 58–65.

(5) Zhao, Y.; Guo, L.; Gándara, F.; Ma, Y.; Liu, Z.; Zhu, C.; Lyu, H.; Trickett, C. A.; Kapustin, E. A.; Terasaki, O.; Yaghi, O. M. A Synthetic Route for Crystals of Woven Structures, Uniform Nanocrystals, and Thin Films of Imine Covalent Organic Frameworks. *J. Am. Chem. Soc.* **2017**, *139*, 13166–13172.

(6) Sasmal, H. S.; Halder, A.; Kunjattu, S. H.; Dey, K.; Nadol, A.; Ajithkumar, T. G.; Ravindra Bedadur, P.; Banerjee, R. Covalent Self-Assembly in Two Dimensions: Connecting Covalent Organic Framework Nanospheres into Crystalline and Porous Thin Films. *J. Am. Chem. Soc.* **2019**, *141*, 20371–20379.

(7) Li, R. L.; Flanders, N. C.; Evans, A. M.; Ji, W.; Castano, I.; Chen, L. X.; Gianneschi, N. C.; Dichtel, W. R. Controlled Growth of Imine-Linked Two-Dimensional Covalent Organic Framework Nanoparticles. *Chem. Sci.* **2019**, *10*, 3796–3801.

(8) Franco, C.; Rodríguez-San-Miguel, D.; Sorrenti, A.; Sevim, S.; Pons, R.; Platero-Prats, A. E.; Pavlovic, M.; Szilágyi, I.; Ruiz Gonzalez, M. L.; González-Calbet, J. M.; Bochicchio, D.; Pesce, L.; Pavan, G. M.; Imaz, I.; Cano-Sarabia, M.; Maspoch, D.; Pané, S.; de Mello, A. J.; Zamora, F.; Puigmartí-Luis, J. Biomimetic Synthesis of Sub-20 Nm Covalent Organic Frameworks in Water. *J. Am. Chem. Soc.* **2020**, *142*, 3540–3547.

(9) Buonsanti, R.; Milliron, D. J. Chemistry of Doped Colloidal Nanocrystals. *Chem. Mater.* **2013**, *25*, 1305–1317.

(10) Huang, J.; Buonsanti, R. Colloidal Nanocrystals as Heterogeneous Catalysts for Electrochemical CO2 Conversion. *Chem. Mater.* **2019**, *31*, 13–25.

(11) Cargnello, M. Colloidal Nanocrystals as Building Blocks for Well-Defined Heterogeneous Catalysts. *Chem. Mater.* **2019**, *31*, 576–596.

(12) Lu, G.; Li, S.; Guo, Z.; Farha, O. K.; Hauser, B. G.; Qi, X.; Wang, Y.; Wang, X.; Han, S.; Liu, X.; Duchene, J. S.; Zhang, H.; Zhang, Q.; Chen, X.; Ma, J.; Loo, S. C. J.; Wei, W. D.; Yang, Y.; Hupp, J. T.; Huo, F. Imparting Functionality to a Metal-Organic Framework Material by Controlled Nanoparticle Encapsulation. *Nat. Chem.* **2012**, *4*, 310–316.

(13) Rungtaweevoranit, B.; Baek, J.; Araujo, J. R.; Archanjo, B. S.; Choi, K. M.; Yaghi, O. M.; Somorjai, G. A. Copper Nanocrystals Encapsulated in Zr-Based Metal-Organic Frameworks for Highly Selective CO2 Hydrogenation to Methanol. *Nano Lett.* **2016**, *16*, 7645–7649.

(14) Zhao, M.; Yuan, K.; Wang, Y.; Li, G.; Guo, J.; Gu, L.; Hu, W.; Zhao, H.; Tang, Z. Metal-Organic Frameworks as Selectivity Regulators for Hydrogenation Reactions. *Nature* **2016**, *539*, 76–80.

(15) Choi, K. M.; Kim, D.; Rungtaweevoranit, B.; Trickett, C. A.; Barmanbek, J. T. D.; Alshammari, A. S.; Yang, P.; Yaghi, O. M. Plasmon-Enhanced Photocatalytic CO2 Conversion within Metal–Organic Frameworks under Visible Light. *J. Am. Chem. Soc.* **2017**, *139*, 356–362.

(16) Yang, Q.; Xu, Q.; Jiang, H. L. Metal – Organic Frameworks Meet Metal Nanoparticles: Synergistic Effect for Enhanced Catalysis. *Chem. Soc. Rev.* **2017**, *46*, 4774–4808.

(17) Yang, X.; Xu, Q. Encapsulating Metal Nanocatalysts within Porous Organic Hosts. *Trends Chem.* **2020**, *2*, 214–226.

(18) Gao, C.; Lyu, F.; Yin, Y. Encapsulated Metal Nanoparticles for Catalysis. *Chem. Rev.* **2021**, *121*, 834–881.

(19) Guntern, Y. T.; Pankhurst, J. R.; Vávra, J.; Mensi, M.; Mantella, V.; Schouwink, P.; Buonsanti, R. Nanocrystal/Metal–Organic Framework Hybrids as Electrocatalytic Platforms for CO2 Conversion. *Angew. Chemie Int. Ed.* **2019**, *58*, 12632–12639.

(20) Osterrieth, J. W. M.; Wright, D.; Noh, H.; Kung, C.-W.; Vulpe, D.; Li, A.; Park, J. E.; Van Duyne, R. P.; Moghadam, P. Z.; Baumberg, J. J.; Farha, O. K.; Fairen-Jimenez, D. Core–Shell Gold Nanorod@Zirconium-Based Metal–Organic Framework Composites as in Situ Size-Selective Raman Probes. *J. Am. Chem. Soc.* **2019**, *141*, 3893–3900.

(21) Pachfule, P.; Panda, M. K.; Kandambeth, S.; Shivaprasad, S. M.; Díaz, D. D.; Banerjee, R. Multifunctional and Robust Covalent Organic Framework-Nanoparticle Hybrids. *J. Mater. Chem. A* **2014**, *2*, 7944–7952.

(22) Pachfule, P.; Kandambeth, S.; Díaz Díaz, D.; Banerjee, R. Highly Stable Covalent Organic Framework-Au Nanoparticles Hybrids for Enhanced Activity for Nitrophenol Reduction. *Chem. Commun.* **2014**, *50*, 3169–3172.

(23) Park, E.; Jack, J.; Hu, Y.; Wan, S.; Huang, S.; Jin, Y.; Maness, P. C.; Yazdi, S.; Ren, Z.; Zhang, W. Covalent Organic Framework-Supported Platinum Nanoparticles as Efficient Electrocatalysts for Water Reduction. *Nanoscale* **2020**, *12*, 2596–2602.

(24) Ma, H. C.; Zhao, C. C.; Chen, G. J.; Dong, Y. Bin. Photothermal Conversion Triggered Thermal

Asymmetric Catalysis within Metal Nanoparticles Loaded Homochiral Covalent Organic Framework. *Nat. Commun.* **2019**, *10*.

(25) Wang, R. L.; Li, D. P.; Wang, L. J.; Zhang, X.; Zhou, Z. Y.; Mu, J. L.; Su, Z. M. The Preparation of New Covalent Organic Framework Embedded with Silver Nanoparticles and Its Applications in Degradation of Organic Pollutants from Waste Water. *Dalt. Trans.* **2019**, *48*, 1051–1059.

(26) Kalidindi, S. B.; Oh, H.; Hirscher, M.; Esken, D.; Wiktor, C.; Turner, S.; Van Tendeloo, G.; Fischer, R. A. Metal@COFs: Covalent Organic Frameworks as Templates for Pd Nanoparticles and Hydrogen Storage Properties of Pd@COF-102 Hybrid Material. *Chem. - A Eur. J.* **2012**, *18*, 10848–10856.

(27) Lu, S.; Hu, Y.; Wan, S.; McCaffrey, R.; Jin, Y.; Gu, H.; Zhang, W. Synthesis of Ultrafine and Highly Dispersed Metal Nanoparticles Confined in a Thioether-Containing Covalent Organic Framework and Their Catalytic Applications. *J. Am. Chem. Soc.* **2017**, *139*, 17082–17088.

(28) Tao, R.; Shen, X.; Hu, Y.; Kang, K.; Zheng, Y.; Luo, S.; Yang, S.; Li, W.; Lu, S.; Jin, Y.; Qiu, L.; Zhang, W. Phosphine-Based Covalent Organic Framework for the Controlled Synthesis of Broad-Scope Ultrafine Nanoparticles. *Small* **2020**, *16*, 1906005.

(29) Tao, R.; Ma, X.; Wei, X.; Jin, Y.; Qiu, L.; Zhang, W. Porous Organic Polymer Material Supported Palladium Nanoparticles. *J. Mater. Chem. A* **2020**, *8*, 17360–17391.

(30) Zhang, Y.; Hu, Y.; Zhao, J.; Park, E.; Jin, Y.; Liu, Q.; Zhang, W. Covalent Organic Framework-Supported Fe–TiO 2 Nanoparticles as Ambient-Light-Active Photocatalysts. *J. Mater. Chem. A* **2019**, *7*, 16364–16371.

(31) Segura, J. L.; Mancheño, M. J.; Zamora, F. Covalent Organic Frameworks Based on Schiff-Base Chemistry: Synthesis, Properties and Potential Applications. *Chem. Soc. Rev.* **2016**, *45*, 5635–5671.

(32) Tan, J.; Namuangruk, S.; Kong, W.; Kungwan, N.; Guo, J.; Wang, C. Manipulation of Amorphous-to-Crystalline Transformation: Towards the Construction of Covalent Organic Framework Hybrid Microspheres with NIR Photothermal Conversion Ability. *Angew. Chemie Int. Ed.* **2016**, *1289*, 14185–14190.

(33) Rodríguez-San-Miguel, D.; Yazdi, A.; Guillerm, V.; Pérez-Carvajal, J.; Puntes, V.; Maspoch, D.; Zamora, F. Confining Functional Nanoparticles into Colloidal Imine-Based COF Spheres by a Sequential Encapsulation–Crystallization Method. *Chem. - A Eur. J.* **2017**, *23*, 8623–8627.

(34) Cui, K.; Zhong, W.; Li, L.; Zhuang, Z.; Li, L.; Bi, J.; Yu, Y. Well-Defined Metal Nanoparticles@Covalent Organic Framework Yolk–Shell Nanocages by ZIF-8 Template as Catalytic Nanoreactors. *Small* **2018**, *15*, 1804419.

(35) Pachfule, P.; Kandmabeth, S.; Mallick, A.; Banerjee, R. Hollow Tubular Porous Covalent Organic Framework (COF) Nanostructures. *Chem. Commun.* **2015**, *51*, 11717–11720.

(36) Shi, X.; Yao, Y.; Xu, Y.; Liu, K.; Zhu, G.; Chi, L.; Lu, G. Imparting Catalytic Activity to a Covalent Organic Framework Material by Nanoparticle Encapsulation. *ACS Appl. Mater. Interfaces* **2017**, *9*, 7481–7488.

(37) Zhang, F.; Yang, Z.; Hao, J.; Zhao, K.; Hua, M.; Yang, Y.; Wei, J. Dynamic Covalent Chemistry Steers Synchronizing Nanoparticle Self-Assembly with Interfacial Polymerization. *Commun. Chem.* **2019**, *2*, 123.

(38) Ding, S. Y.; Gao, J.; Wang, Q.; Zhang, Y.; Song, W. G.; Su, C. Y.; Wang, W. Construction of Covalent

Organic Framework for Catalysis: Pd/COF-LZU1 in Suzuki-Miyaura Coupling Reaction. *J. Am. Chem. Soc.* **2011**, *133*, 19816–19822.

(39) Fan, H.; Gu, J.; Meng, H.; Knebel, A.; Caro, J. High-Flux Membranes Based on the Covalent Organic Framework COF-LZU1 for Selective Dye Separation by Nanofiltration. *Angew. Chemie Int. Ed.* **2018**, *57*, 4083–4087.

(40) Yao, T.; Cui, T.; Wang, H.; Xu, L.; Cui, F.; Wu, J. A Simple Way to Prepare Au@polypyrrole/Fe3O4 Hollow Capsules with High Stability and Their Application in Catalytic Reduction of Methylene Blue Dye. *Nanoscale* **2014**, *6*, 7666–7674.

(41) Sahiner, N.; Sagbas, S.; Aktas, N. Very Fast Catalytic Reduction of 4-Nitrophenol, Methylene Blue and Eosin y in Natural Waters Using Green Chemistry: P(Tannic Acid)-Cu Ionic Liquid Composites. *RSC Adv.* **2015**, *5*, 18183–18195.

(42) Wiktor, C.; Meledina, M.; Turner, S.; Lebedev, O. I.; Fischer, R. A. Transmission Electron Microscopy on Metal-Organic Frameworks-a Review. *J. Mater. Chem. A* **2017**, *5*, 14969–14989.

(43) Zhang, D.; Zhu, Y.; Liu, L.; Ying, X.; Hsiung, C. E.; Sougrat, R.; Li, K.; Han, Y. Atomic-Resolution Transmission Electron Microscopy of Electron Beam–Sensitive Crystalline Materials. *Science* **2018**, *359*, 675–679.

(44) Wang, H.; He, B.; Liu, F.; Stevens, C.; Brady, M. A.; Cai, S.; Wang, C.; Russell, T. P.; Tan, T. W.; Liu, Y. Orientation Transitions during the Growth of Imine Covalent Organic Framework Thin Films. *J. Mater. Chem. C* **2017**, *5*, 5090–5095.

(45) Gao, Q.; Bai, L.; Zeng, Y.; Wang, P.; Zhang, X.; Zou, R.; Zhao, Y. Reconstruction of Covalent Organic Frameworks by Dynamic Equilibrium. *Chem. - A Eur. J.* **2015**, *21*, 16818–16822.

(46) Smith, B. J.; Overholts, A. C.; Hwang, N.; Dichtel, W. R. Insight into the Crystallization of Amorphous Imine-Linked Polymer Networks to 2D Covalent Organic Frameworks. *Chem. Commun.* **2016**, *52*, 3690–3693.

(47) Feriante, C.; Evans, A. M.; Jhulki, S.; Castano, I.; Strauss, M. J.; Barlow, S.; Dichtel, W. R.; Marder, S. R. New Mechanistic Insights into the Formation of Imine-Linked Two-Dimensional Covalent Organic Frameworks. *J. Am. Chem. Soc.* **2020**, *142*, 18637–18644.

(48) Yuan, Y.-C.; Sun, B.; Cao, A.-M.; Wang, D.; Wan, L.-J. Heterogeneous Nucleation and Growth of Highly Crystalline Imine-Linked Covalent Organic Frameworks. *Chem. Commun.* **2018**, *54*, 5976–5979.

(49) Kandambeth, S.; Venkatesh, V.; Shinde, D. B.; Kumari, S.; Halder, A.; Verma, S.; Banerjee, R. Self-Templated Chemically Stable Hollow Spherical Covalent Organic Framework. *Nat. Commun.* **2015**, *6*, 1–10.

(50) Lu, Z.; Liu, Y.; Liu, X.; Lu, S.; Li, Y.; Yang, S.; Qin, Y.; Zheng, L.; Zhang, H. A Hollow Microshuttle-Shaped Capsule Covalent Organic Framework for Protein Adsorption. *J. Mater. Chem. B* **2019**, *7*, 1469–1474.

(51) Gropp, C.; Canossa, S.; Wuttke, S.; Gándara, F.; Li, Q.; Gagliardi, L.; Yaghi, O. M. Standard Practices of Reticular Chemistry. *ACS Cent. Sci.* **2020**, *6*, 1255–1273.

(52) Miao, Y. E.; Lee, H. K.; Chew, W. S.; Phang, I. Y.; Liu, T.; Ling, X. Y. Catalytic Liquid Marbles: Ag Nanowire-Based Miniature Reactors for Highly Efficient Degradation of Methylene Blue. *Chem. Commun.* **2014**, *50*, 5923–5926.

(53) Jana, N. R.; Sau, T. K.; Pal, T. Growing Small Metal Particle as Redox Catalyst. *J. Phys. Chem. B* **1999**, *103*, 115–121.

(54) Ghosh, S. K.; Kundu, S.; Mandal, M.; Pal, T. Silver and Gold Nanocluster Catalyzed Reduction of Methylene Blue by Arsine in a Micellar Medium. *Langmuir* **2002**, *18*, 8756–8760.

(55) Kandambeth, S.; Mallick, A.; Lukose, B.; Mane, M. V.; Heine, T.; Banerjee, R. Construction of Crystalline 2D Covalent Organic Frameworks with Remarkable Chemical (Acid/Base) Stability via a Combined Reversible and Irreversible Route. *J. Am. Chem. Soc.* **2012**, *134*, 19524–19527.

(56) Saris, S.; Loiudice, A.; Mensi, M.; Buonsanti, R. Exploring Energy Transfer in a Metal/Perovskite Nanocrystal Antenna to Drive Photocatalysis. *J. Phys. Chem. Lett.* **2019**, *10*, 7797–7803.

(57) Xie, C.; Chen, C.; Yu, Y.; Su, J.; Li, Y.; Somorjai, G. A.; Yang, P. Tandem Catalysis for CO2 Hydrogenation to C2 –C4 Hydrocarbons. *Nano Lett.* **2017**, *17*, 3798–3802.

(58) Lin, L.; Liu, T.; Xiao, J.; Li, H.; Wei, P.; Gao, D.; Nan, B.; Si, R.; Wang, G.; Bao, X. Enhancing CO2 Electroreduction to Methane with a Cobalt Phthalocyanine and Zinc–Nitrogen–Carbon Tandem Catalyst. *Angew. Chemie Int. Ed.* **2020**, *59*, 22408–22413.